RAA 2021 Vol. **21** No. **11**, 289(9pp) doi:10.1088/1674-4527/21/11/289

http://www.raa-journal.org *http://iopscience.iop.org/raa*

***R**esearch in*
***A**stronomy and*
***A**strophysics*

X-ray source population in the polar ring galaxy NGC 660 as observed by *Chandra*

Nurnabilah Nazri and Adlyka Annuar*

Department of Applied Physics, Faculty of Science and Technology, Universiti Kebangsaan Malaysia, 43600 UKM Bangi, Selangor, Malaysia; *adlyka@ukm.edu.my*

Received 2021 May 6; accepted 2021 August 15

Abstract We present *Chandra* observations of the nearby polar ring galaxy NGC 660 to study its X-ray source population. Based on our analysis, we detected a total of 23 X-ray sources in the 0.5−8 keV band, with luminosities ranging from $\sim 10^{37}$ to $\sim 10^{39}$ erg s^{-1}. Twenty-two of these sources are located off-nuclear and have luminosities below the ultraluminous X-ray source (ULX) threshold value of $L_{0.5-8\,\mathrm{keV}} < 10^{39}$ erg s^{-1}, suggesting that they are likely to be X-ray binary (XRB) candidates. The remaining source is located at the center of the galaxy, suggesting it is an active galactic nucleus (AGN). However, we estimated that four of the detected sources could be associated with background objects. Based on the source count rates in each of the *Chandra* observations, we found evidence for variability in nine of the 23 sources, including the AGN. However, further investigation with spectral analysis suggested no significant differences in the AGN luminosities between the observations. The X-ray luminosity distribution of the galaxy was found to be generally lower than that expected from previous studies on star forming and collisional ring galaxies. No ULX was also detected in the galaxy, in contrast with what was expected from the galaxy's SFR and metallicity (i.e., SFR = $14.43 \pm 0.19\ M_{\odot}$ yr^{-1} and $Z = 0.94 \pm 0.01\ Z_{\odot}$, respectively). These results suggest a deficit in the X-ray sources detected. Based on source hardness ratio distribution, we found evidence that the fainter sources have a harder source spectrum, indicating higher absorption. This further suggests that there could be more X-ray sources that were not detected in the galaxy due to significant obscuration.

Key words: Galaxies: individual: NGC 660 — X-rays: individual: NGC 660 — Galaxies: active

1 INTRODUCTION

Astronomical X-ray sources such as X-ray binaries (XRBs), ultra-luminous X-ray (ULX) sources and active galactic nuclei (AGNs) have been observed and studied in different types of galaxies including starbursts (e.g., Ducci et al. 2013; Sanchez & Rangelov 2019 and Vulic et al. 2020), galaxy pairs (e.g., Roberts et al. 2002; Mineo et al. 2014) and star-forming galaxies (e.g., Liu et al. 2019). Most X-ray emission detected from these galaxies comes from the central AGN (Zadorozhna L. V. et al. 2020). Unfortunately, no such study has been done specifically on polar-ring galaxies (PRGs). This type of galaxy possesses unique and picturesque features in which an outer ring of gas and stars rotates over the pole of the galaxy (Smirnova et al. 2017). In most cases, the disks of the galaxies are poor in gas while the ring is commonly dominated by younger and bluish stars (Reshetnikov & Mosenkov 2019). Although PRGs account for only a fraction of $\sim 10^{-3}$ of all galaxies in the local Universe (Whitmore et al. 1990; Reshetnikov et al. 2011; and Mosenkov et al. 2018), new PRG candidates have been increasingly identified in recent years (Reshetnikov & Mosenkov 2019).

In this paper, we will focus on a nearby PRG, NGC 660 (Whitmore et al. 1990), which is located at a distance of 12.3 Mpc (Goulding & Alexander 2009), as a case study of X-ray source population in a PRG. NGC 660 is reported to be a rare PRG since it is a late-type galaxy, i.e., Sa-type (Goulding & Alexander 2009), which is in contrast with most PRGs. Early studies on the galaxy showed a prominent feature of different molecular gas distribution, which is 10× more concentrated in the disk as compared to the ring of the galaxy (van Driel et al. 1995). This is further supported by a recent study using infrared (IR) and ultraviolet (UV) observations, in which it was found that the disk of NGC 660 is brighter in IR, where richer and heavier dust particles in the disk are heated

* Corresponding author

Table 1 *Chandra* Observation Log for NGC 660

Observation (1)	Date (2)	Exposure time (ks) (3)
1633	2001 January 28	1.94
4010	2003 February 22	5.13
15333	2012 November 20	28.06
15587	2012 December 18	23.06
18352	2015 August 26	10.12

Column (1): Observation identification number; (2): Observation UT start date; (3): On-source exposure time in ks.

by UV radiation to generate more intense IR emission as compared to the ring (Smirnova et al. 2017). These high columns of dust and gas could trigger a high star formation rate (SFR) in the galaxy, which is an important factor in determining the total number of X-ray sources in the galaxy, specifically XRBs (Fabbiano 2019). Indeed, it has been shown that SFR correlates with the number of X-ray sources in galaxies (Mineo et al. 2014).

An AGN has been identified in NGC 660 in various wavelengths. In 2009, the AGN was detected using the high ionization [NeV]λ 14.32 µm emission line (ionization energy = 97.1 eV) at the center of the galaxy (Goulding & Alexander 2009). This was then further strengthened by a high resolution radio observation with e-MERLIN in 2013 in which a spectacular radio outburst at the central region of the galaxy was seen (Argo et al. 2015). A more recent study by Annuar et al. (2020) using low and high energy X-ray observations from *Chandra* and *NuSTAR*, respectively, as well as mid-IR continuum observation from the *Very Large Telescope* (VLT) VISIR, also clearly detected the AGN. In addition, they also found that the AGN is actually a low luminosity heavily obscured AGN, potentially Compton-thick, with an intrinsic luminosity of $L_{\rm int,\,2-10\,keV} \gtrsim 5.75 \times 10^{39}$ erg s^{-1} and torus column density of $\log N_{\rm H} \gtrsim 23.78$ cm^{-2}.

NGC 660 has been observed in X-rays multiple times. The first X-ray observation was done by *ROSAT* in 1992, followed by *Chandra* and *XMM-Newton* in 2001, and more recent observations have been made with *Chandra*, *NuSTAR* and the *Neil Gehrels Swift* telescope. In this paper, we will use X-ray observations specifically from *Chandra* to study the X-ray source population in the galaxy, due to the higher angular resolution of *Chandra* ($\sim$ 0.5 arcsec) as compared to other X-ray telescopes. We detail all of the *Chandra* observations for the galaxy, and the data reduction procedures adopted in this work in Section 2. We present the X-ray source detection analysis and results in Section 3. In Sections 4 and 5, we investigate the hardness ratios (HRs) and variability of the X-ray sources, respectively. This is followed by spectral analysis of the sources in Section 6. Finally in Sections 7 and 8, we present our discussion and conclusion, respectively.

2 *CHANDRA* OBSERVATIONS

NGC 660 was observed by *Chandra* five times from 2001 until 2015. In all observations, the whole galaxy was within the field-of-view of *Chandra*. We detail each of the *Chandra* observations in Table 1. Our data reduction procedure was performed employing CIAO version 4.11 and CALDB version 4.8.4. We first reprocessed the data executing the CHANDRA_REPRO task to create a cleaned event file and new pixel file with updated calibration modification. We then ran the MERGED_OBS task to reproject and combine multiple observations to create a merged event file and exposure-corrected image. The merged event file created has a total net exposure time $t_{\rm exp} = 67.5$ ks. Event files at different energy bands, i.e., 0.5–8.0 keV (full), 0.5–2 keV (soft) and 2–8 keV (hard), were then created using the DMCOPY task.

3 X-RAY SOURCE DETECTION

The X-ray source detection was performed utilizing the WAVDETECT task on the full, hard and soft band merged event files at 1, 2, 4 and 16 pixels. The detected X-ray sources were then overlapped on top of an optical image of NGC 660 obtained from the Sloan Digital Sky Survey (SDSS) in the g, r and i bands (Baillard et al. 2011). Visual examination was done to identify the sources that are located within the optical boundary of the galaxy determined by contour analysis (contour level =13, contour smoothness =2).

Using the full band data, we identified a total of 23 X-ray sources within the optical boundary of NGC 660, of which 16 sources were detected in the soft band only, 15 sources in the hard band only and four sources were undetected in both bands. The X-ray and optical images of the galaxy are displayed in Figure 1, with sources detected in the galaxy in the full band marked. The properties of the sources including positions, count rates, fluxes and luminosities are tabulated in Table 2.

The source fluxes were determined based on their detected count rates utilizing the Portable Interactive Multi-Mission Simulator (WEBPIMMS)[1] assuming a simple power-law model, with a photon index of $\Gamma = 1.9$ and Galactic absorption $N_{\rm H} = 4.64 \times 10^{20}$ cm^{-2} (Kalberla et al. 2005). The source luminosities were then calculated based on the measured fluxes, assuming that they are located within NGC 660.

Based on the calculated luminosities and source positions, we classified the sources into XRB, ULX and AGN candidates. Off-nuclear sources with $L_{0.5-8\,\rm keV} \geq 10^{39}$ erg s^{-1} were classified as XRB candidates and those with $L_{0.5-8\,\rm keV} \geq 10^{39}$ erg s^{-1} were categorized as ULX

[1] https://heasarc.gsfc.nasa.gov/cgi-bin/Tools/w3pimms/w3pimms.pl

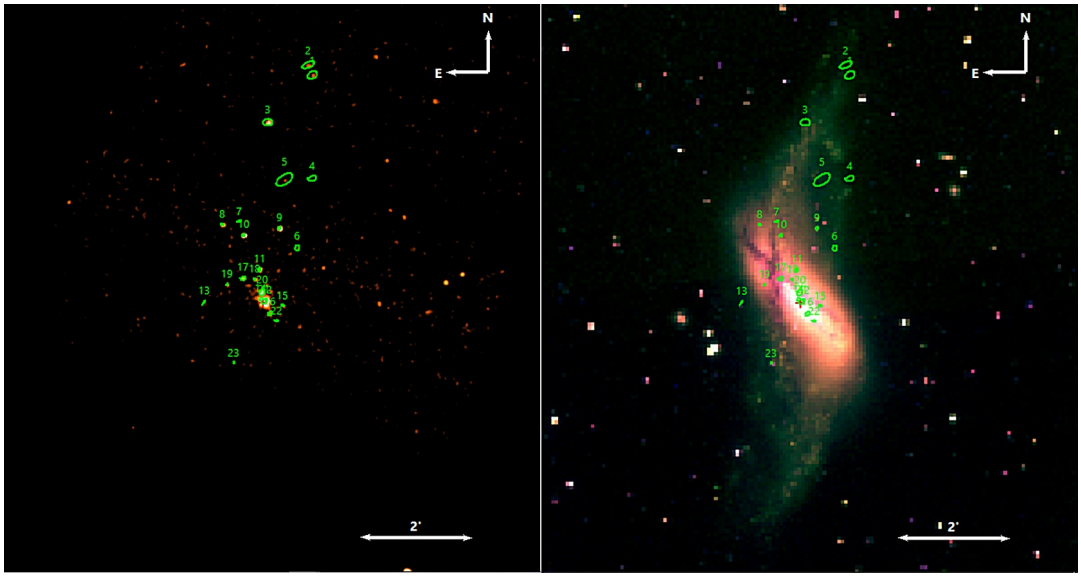

Fig. 1 X-ray (0.5–8 keV) and optical (g, r and i) images of NGC 660 taken by *Chandra* (*left*) and ESO DSS (*right*), respectively. The X-ray sources detected in the galaxy are marked with green circular regions. The size of the region indicates the 90% enclosed count fraction for the detected source. The center of the galaxy is marked with a red plus sign. The X-ray image has been smoothed with a Gaussian function of radius 2 pixels for visual clarity.

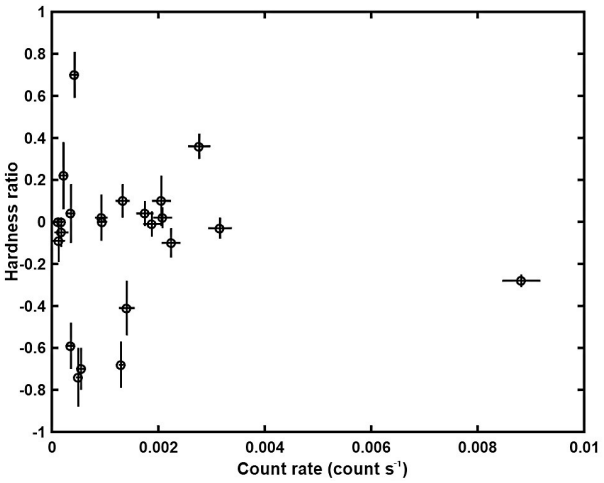

Fig. 2 HR as a function of count rates, $CR_{0.5-8\ \mathrm{keV}}$ (count s^{-1}), for sources detected in NGC 660.

candidates. We determined that 22 of the sources are XRB candidates and one is highly likely to be the AGN (source 21) since it is located at the center of the galaxy, i.e., RA = 01:43:02.3391 and Dec = 13:38:44.115, consistent with the radio position found by Argo et al. (2015). Although the luminosity calculated for the AGN is relatively low (i.e., $\log L_{\mathrm{obs,\ 0.5-8\ keV}} = 39.26 \pm 0.02$ erg s^{-1}), this has been acknowledged in past study which identified it as a low luminosity heavily obscured AGN (Annuar et al. 2020). Meanwhile for the 22 XRB candidates, their luminosities range between $\sim \log(37 - 38)$ erg s^{-1} and no ULX candidate was identified.

3.1 Background Sources

We would expect that some percentage of the X-ray sources detected are actually background sources. We therefore determined the fraction of background contamination in the galaxy by utilizing the *Chandra* Deep Field-South cumulative number counts and photon index power-law model from Luo et al. (2017), based on the number of sources detected in the soft and hard bands earlier.

The limiting count rates detected from our analysis in the hard and soft bands are 2.37×10^{-4} count s^{-1} and 3.71×10^{-4} count s^{-1}, respectively. These translate to limiting fluxes of 7.75×10^{-15} erg s^{-1} cm^{-2} and 2.03×10^{-15} erg s^{-1} cm^{-2} for the hard and soft bands, respectively, assuming a power-law model with Γ = 1.4 (Luo et al. 2017). Based on Luo et al. (2017), these values correspond to 712 and 792 sources per square degree, respectively.

We then calculated the total area of NGC 660 using measured diameters from the K-band near-IR data observed by the Two Micron All Sky Survey (2MASS) reported in Jarrett et al. (2003) in order to determine the level of background contamination in the galaxy. Based on this, we estimated total contamination levels of $<$1.9 and $<$2.2 cosmic background sources for the hard and soft bands, respectively, over the total area of 2.72×10^{-3} square degrees. These threshold values convert less than 13% and 12% of the detections in the hard and soft bands, respectively. Overall, the total sum of X-ray background sources detected in both bands, i.e., the full band, is four sources.

Table 2 X-ray Sources Detected in NGC 660 by *Chandra*

Source ID (1)	RA h m s (2)	Dec d m s (3)	$CR_{0.5-8\mathrm{keV}}$ $\times10^{-3}$ cts s^{-1} (4)	$f_{0.5-8\mathrm{keV}}$ $\times10^{-14}$ erg s^{-1} cm^{-2} (5)	log $L_{0.5-8\mathrm{keV}}$ erg s^{-1} (6)	HR (7)	Classification (candidates) (8)
1	1:42:58.7358	+13:42:48.190	1.33 ± 0.13	1.63 ± 0.17	38.44 ± 0.04	0.10 ± 0.08	XRB
2	1:42:59.0330	+13:42:59.050	1.41 ± 0.15	1.72 ± 0.18	$38.47^{+0.04}_{-0.05}$	-0.41 ± 0.13 †	XRB
3	1:43:02.0201	+13:41:57.193	2.53 ± 0.18	2.53 ± 0.22	38.63 ± 0.04	0.02 ± 0.05	XRB
4	1:42:58.7448	+13:40:56.793	0.36 ± 0.07	0.43 ± 0.09	$37.87^{+0.08}_{-0.10}$	-0.59 ± 0.11 †	XRB
5	1:43:00.8100	+13:40:55.544	2.06 ± 0.18	2.52 ± 0.22	38.63 ± 0.02	0.10 ± 0.12 †	XRB
6	1:42:59.8472	+13:39:41.838	0.43 ± 0.07	0.53 ± 0.09	$37.95^{+0.07}_{-0.08}$	0.70 ± 0.11 †	XRB
7	1:43:04.1501	+13:40:10.695	0.22 ± 0.06	0.27 ± 0.07	$37.66^{+0.07}_{-0.08}$	0.22 ± 0.16 †	XRB
8	1:43:05.3873	+13:40:06.921	0.93 ± 0.12	1.14 ± 0.15	$38.29^{+0.05}_{-0.06}$	0.02 ± 0.11	XRB
9	1:43:01.1671	+13:40:03.349	1.75 ± 0.16	2.14 ± 0.20	38.56 ± 0.04	0.04 ± 0.06	XRB
10	1:43:03.8274	+13:39:55.799	3.16 ± 0.22	3.86 ± 0.27	38.82 ± 0.03	-0.03 ± 0.05	XRB
11	1:43:01.3610	+13:38:23.429	0.18 ± 0.04	0.22 ± 0.05	$37.57^{+0.10}_{-0.12}$	-0.05 ± 0.07	XRB
12	1:43:02.1186	+13:38:45.791	1.88 ± 0.16	2.30 ± 0.20	38.59 ± 0.04	-0.01 ± 0.06	XRB
13	1:43:06.7500	+13:38:43.702	0.12 ± 0.04	0.15 ± 0.05	$37.39^{+0.14}_{-0.20}$	0.00 †	XRB
14	1:43:02.5320	+13:38:46.767	2.77 ± 0.21	3.38 ± 0.26	38.76 ± 0.03	0.36 ± 0.06	XRB
15	1:43:00.9140	+13:38:40.087	0.18 ± 0.04	0.22 ± 0.05	$37.57^{+0.10}_{-0.12}$	0.00 †	XRB
16	1:43:01.8514	+13:38:31.260	0.55 ± 0.09	0.67 ± 0.11	$38.06^{+0.07}_{-0.08}$	-0.70 ± 0.10 †	XRB
17	1:43:04.5270	+13:37:38.338	0.13 ± 0.04	0.16 ± 0.05	$37.44^{+0.12}_{-0.18}$	-0.09 ± 0.10 †	XRB
18	1:43:03.8469	+13:39:09.015	0.95 ± 0.12	1.16 ± 0.15	$38.29^{+0.05}_{-0.06}$	0.00	XRB
19	1:43:05.0361	+13:39:02.815	0.36 ± 0.07	1.16 ± 0.15	$38.87^{+0.08}_{-0.10}$	0.04 ± 0.14	XRB
20	1:43:02.4468	+13:38:54.016	2.24 ± 0.18	0.43 ± 0.09	$38.67^{+0.03}_{-0.04}$	-0.10 ± 0.07	XRB
21	1:43:02.3391	+13:38:44.115	8.82 ± 0.36	2.73 ± 0.22	39.26 ± 0.02	-0.28 ± 0.03	AGN
22	1:43:02.6390	+13:39:18.899	1.30 ± 0.13	1.59 ± 0.16	$38.43^{+0.04}_{-0.05}$	-0.68 ± 0.11 †	XRB
23	1:43:02.9920	+13:39:08.236	0.50 ± 0.09	0.61 ± 0.11	$38.02^{+0.07}_{-0.08}$	-0.74 ± 0.14 †	XRB

Column (1): Identification number (ID) of the detected X-ray sources; (2)–(3): right ascension (RA) and declination (Dec) of the sources; (4): Detected count rates in 0.5–8 keV band; (5)–(6): Absorbed 0.5–8 keV fluxes and luminosities determined from the count rates using WEBPIMMS; (7): HR (†calculated from aperture-based net counts); and (8) Classification of the sources on the basis of their measured luminosities.

Table 3 HR distribution for X-ray sources detected in NGC 660. The four sources which were not detected in both soft and hard bands were excluded from this analysis.

Sample	Num. of sources	CR limits (count s^{-1})	Range of HR values	Median HR
Bright	1	> 3.16	–0.28	–0.28
Medium	14	$0.43 - 3.16$	$-0.70 - 0.36$	0.00
Faint	4	< 0.43	$-0.59 - 0.70$	0.13

4 HARDNESS RATIO

In this section, we study the HR distribution of the detected X-ray sources. We calculated the HR of each source using equation (1) of Mineo et al. (2014). For sources which were not detected in the soft and/or hard bands (see Sect. 3), we obtained the photon counts utilizing aperture photometry. We used the source regions obtained from the full band detection analysis, and annulus background region to determine the net counts for the sources.

We present the HR distribution for the sources in Table 3 and Figure 2. In Table 3, we separate the sources into three samples, i.e., bright, medium and faint, based on the count rate limits of $> 3.16 \times 10^{-3}$ count s^{-1} for bright, $(0.43 - 3.16) \times 10^{-3}$ count s^{-1} for medium and $< 0.43 \times 10^{-3}$ count s^{-1} for faint sources. These count rate limits correspond to luminosities of $> 10^{39}$ erg s^{-1}, $(10^{38} - 10^{39})$ erg s^{-1} and $< 10^{38}$ erg s^{-1}, respectively. Based on Table 3, we can see that as the count rate decreases (from brighter to fainter sample), the median value of the HR increases. Since a more positive value of HR indicates a harder source spectrum, this result suggests that the fainter sources are more absorbed than their brighter counterparts. Based on Figure 2, we can also see that the brightest source detected has softer HR as compared to most of the fainter sources detected.

5 X-RAY VARIABILITY

In this section, we investigate the X-ray variability for the sources detected in NGC 660. In order to do this, we analyzed each of the five *Chandra* observations individually. We ran the WAVDETECT task to detect the X-ray sources in each observation. However, some sources were not detected in some of the observations, which can be evidence for variability, or merely due to shorter exposure times. Therefore for the undetected sources, we determined the upper limit count rates using aperture

Table 4 Count Rates Detected in Each *Chandra* Observation for All Sources

	Observation ID	1633	4010	15 333	15 587	18 352
	Observation Date	January 2001	February 2003	November 2012	December 2012	August 2015
	Exposure time (ks)	1.92	5.07	28.06	23.06	10.12
	X-ray Source ID		$CR_{0.5-8\ \mathrm{keV}}$	($\times 10^{-3}$	count s^{-1})	
Variable Source Candidates	1	<2.61	0.79 ± 0.39	0.53 ± 0.13	0.51 ± 0.14	<0.30
	2	<1.04†	<0.99	0.44 ± 0.13	0.65 ± 0.14	<0.20
	3	<1.57	<0.99	1.58 ± 0.26	1.55 ± 0.25	2.00 ± 0.50
	7	<1.04 †	<0.2†	0.40 ± 0.13	<0.11	<0.20
	8	<1.57	1.38 ± 0.59	0.88 ± 0.18	1.16 ± 0.22	<0.70
	9	2.09 ± 1.04	2.76 ± 0.79	1.32 ± 0.22	1.44 ± 0.22	2.40 ± 0.50
	11	<1.04†	<0.59	1.27 ± 0.26	1.16 ± 0.22	1.20 ± 0.30
	12	<3.65	4.34 ± 0.59	1.76 ± 0.26	1.52 ± 0.22	<2.10
	21	8.35 ± 2.09	4.73 ± 1.38	9.01 ± 0.62	8.27 ± 0.54	<8.80
Non-variable Source Candidates	4	<1.04†	<0.59	<0.31	<0.25	<0.2†
	5	<1.57	<0.9	0.40 ± 0.13	<1.05	<0.20
	6	<1.04	<0.2†	<0.26	0.29 ± 0.11	<0.20
	10	2.61 ± 1.04	2.76 ± 0.79	2.99 ± 0.35	3.00 ± 0.32	2.20 ± 0.50
	13	<1.04	<0.2†	<0.13	<0.18	<0.2†
	14	3.65 ± 1.04	<2.96	2.94 ± 0.40	<2.60	<2.90
	15	<1.04	<0.2†	<0.13	<0.22	<0.2†
	16	<1.04	0.39 ± 0.20	0.62 ± 0.18	<0.25	<0.30
	17	<1.04†	<0.99	0.70 ± 0.18	0.87 ± 0.18	0.80 ± 0.30
	18	<2.61	0.59 ± 0.20	0.40 ± 0.13	0.47 ± 0.14	<0.50
	19	<1.04	<0.59	0.40 ± 0.13	0.22 ± 0.07	<0.60
	20	<2.61	3.16 ± 0.79	2.06 ± 0.31	1.55 ± 0.25	1.00 ± 0.30
	22	<1.04†	0.2 ± 0.02	<0.26	<0.18	<0.30
	23	<1.04†	<0.2†	0.04 ± 0.04	0.14 ± 0.07	<0.20

† Limiting count rate of the particular observation due to zero photon detection.

photometry utilizing the source regions obtained from the merged observation detection. For those with zero photon counts, we use the limiting count rates in each observation as the upper limits. We tabulated the source count rates for each observation in Table 4.

Based on our analysis, we found that nine of the sources exhibit significant X-ray variability (see Table 4) due to the presence of significant differences in their count rates among the five observations. For sources 1, 2 and 8, the count rates are consistent within error between 2001 and 2012. The count rates then significantly drop in 2015, and in fact the three sources were not detected in this observation. Similar results were found for sources 9 and 12 in which the count rates are consistent between 2001 and 2003, but then decrease significantly in 2012. However for source 9, the count rate slightly increased in 2015. Meanwhile, source 7 was not detected in all of the observations except for one which was conducted in November 2012. In fact, the source count rates in the two observations taken in 2012 over a month apart, with similar exposure times, show a significant difference, in which the count rate drops by more than half in the latter observation and the source went back to not being detected. For sources 3 and 11, the count rates slightly increase between the years 2003 and 2012, and then remained consistent until the last observation in 2015.

Meanwhile, the AGN, i.e., source 21, displayed consistent values in count rates throughout the five observations, except in 2003, where there was a $\sim 50\%$ drop in count rates with respect to the earlier observation taken in 2001. The count rates then rose again in 2012 to the values that are consistent with the 2001 observation.

6 X-RAY SPECTRAL ANALYSIS

In this section we further investigate the properties of the detected sources applying X-ray spectral analysis. However, we only performed the analysis on sources with sufficient number of counts, i.e., >200 counts in the combined observations, in order to get reliable results. Unfortunately, there are only two sources that meet this criterion; i.e, sources 10 and 21 (the AGN). We extracted the spectra for each observation using the SPECEXTRACT task in CIAO, and then combined the spectra using the COMBINE_SPECTRA task. The spectra were then grouped into 20 counts per bin to allow the chi-squared χ^2 statistic to be used, unless stated otherwise. The spectra were then fitted utilizing the X-ray spectral fitting package, XSPEC version 12.10.1. The redshift used in all fittings was fixed at $z = 0.00283$ (Lu et al. 1993). A fixed Galactic absorption component, $N_{\mathrm{H}}^{\mathrm{Gal}} = 4.64 \times 10^{20}$ cm^{-2} (Kalberla et al. 2005) was also included in all spectral fittings.

Table 5 X-ray Spectral Fitting Results for Source 10

Parameter	Unit	PHABS*TBABS*ZPOWERLW	PHABS*TBABS*DISKBB
$N_{\rm H}$	$\times 10^{22}$ cm^{-2}	<0.35	<0.09
Γ	...	$1.54^{+2.15}_{-1.22}$	...
Tin	keV	...	$1.56^{+2.27}_{-1.60}$
$\log L_{0.5-8{\rm keV}}$	erg s^{-1}	$38.69^{+0.07}_{-0.16}$	38.63 ± 0.05
χ^2_r	...	1.15	1.75

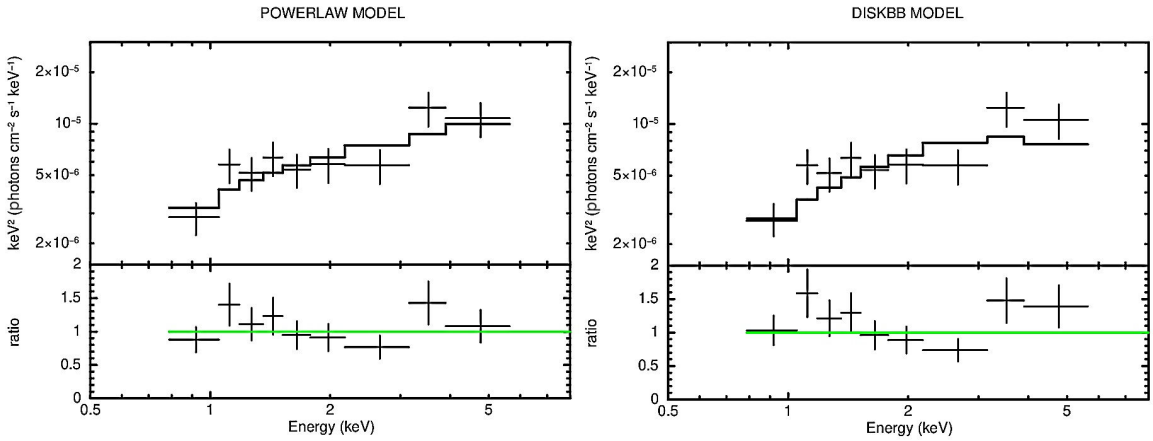

Fig. 3 Best fit spectra for Source 10 applying the POWERLAW model (*left*) and the DISKBB model (*right*). The top panel for each plot indicates the data and unfolded model, while the bottom panel plots the ratio between the data and the folded model.

6.1 Source 10 (Off-Nuclear Source)

We extracted the spectra for source 10 from each observation using a 2″-radius circular region, and annulus region of 2″ and 12″ inner and outer radii, respectively, for the background, centered on the source. We first fitted the spectra with a simple powerlaw model (ZPOWERLW), absorbed by a column density intrinsic to the source (TBABS) and the Galactic absorption (PHABS). We were able to obtain a good fit to the data with $\chi^2_{\rm r}$ = 1.15. The intrinsic column density component, however, was not constrained with an upper limit value of $N_{\rm H} < 0.35 \times 10^{22}$ cm^{-2}, suggesting poor obscuration. The photon index value measured was $\Gamma = 1.54^{+2.15}_{-1.22}$, consistent with values obtained for other XRBs in previous studies (e.g., Bozzo et al. 2012 and Sharma et al. 2020).

We then fitted the spectra with a multicolor disk model (DISKBB), which also gave an acceptable fit albeit slightly poorer than the powerlaw model, i.e., $\chi^2_{\rm r}$ = 1.75. The values obtained for the intrinsic column density and inner disk temperature are $N_{\rm H} < 0.09 \times 10^{22}$ cm^{-2} and $T_{\rm in} = 1.56^{+2.27}_{-1.60}$ keV, respectively.

The best fit spectra and results for both models are displayed in Figure 3 and Table 5, respectively. The absorbed luminosities measured from both spectral fittings are consistent with those calculated from the source count rates (see Table 2), and are below the threshold luminosity value for a ULX, supporting our initial classification that the source is likely to be an XRB.

6.2 Source 21 (AGN)

Based on the count rates detected from each of the *Chandra* observations, the AGN (source 21) displays consistent values throughout the five observations, except for the one taken in February 2003. We investigated this variability further by performing X-ray spectral analysis for each observation. The spectra were extracted using circular regions of 2.8″ and 20″-radii for the source and background respectively. The background was extracted from a source-free region close to the AGN. All spectra were grouped into 1 count per bin due to limited number of counts, and the fits were optimized using the C-statistic.

We modeled each spectrum using a simple absorbed power-law model, in addition to a Gaussian component for the 2012 observations due to the presence of an emission line at ∼6.4 keV, possibly associated with an iron Kα line. Based on our analysis, we obtained consistent values for all parameters, including the photon index, intrinsic column density and luminosity, with the exception of the 2003 observation, i.e., ObsID 4010. We therefore proceeded to combine the four consistent spectra together (i.e., ObsID 1633, 15333, 15578 and 18352), and performed spectral fittings on the combined spectrum to further

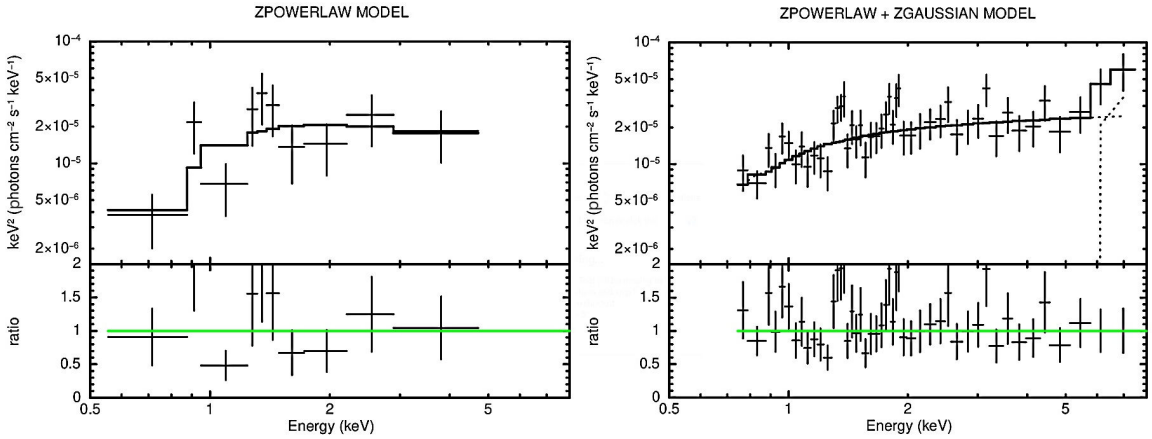

Fig. 4 Best fit spectra for the AGN (Source 21) using POWERLAW model for $\mathrm{AGN}_{1\ \mathrm{OBS}}$ (*left*) and $\mathrm{AGN}_{4\ \mathrm{OBS}}$ (*right*). The top panel for each plot indicates the data and unfolded model, while the bottom panel shows the ratio between the data and the folded model. The data for $\mathrm{AGN}_{1\ \mathrm{OBS}}$ were rebinned to 2σ significance with a maximum of 100 counts per bin for visual clarity.

investigate the variability between these four observations (hereafter $\mathrm{AGN}_{4\ \mathrm{OBS}}$) and the 2003 observation (hereafter $\mathrm{AGN}_{1\ \mathrm{OBS}}$).

We fitted both spectra using an absorbed simple power-law model as follows: (PHABS* ZWABS* ZPO). For the $\mathrm{AGN}_{4\ \mathrm{OBS}}$ spectrum, we observed significant fit residuals at ∼6.4 keV which is likely associated with the presence of the iron Kα emission line. We therefore added a Gaussian component (i.e., ZGAU) to the model to simulate this line. Our best fit spectral modelings for both spectra are depicted in Figure 4 spectra and results for both models are presented in Figure 4 and Table 6, respectively. Based on our fittings, the photon indices measured for both spectra are consistent with each other within the statistical uncertainties, i.e., $\Gamma = 1.71^{+0.32}_{-0.30}$ and $\Gamma = 2.50^{+1.14}_{-1.00}$ for $\mathrm{AGN}_{4\ \mathrm{OBS}}$ and $\mathrm{AGN}_{1\ \mathrm{OBS}}$, respectively. These values also agree with the typical value measured for a Swift-BAT AGN (i.e., $\Gamma \sim 1.8$; Ricci et al. 2017).

The intrinsic column densities measured are also consistent with each other, i.e., $N_{\mathrm{H}} = 0.42\ ^{+0.40}_{-0.33}$ and $N_{\mathrm{H}} = 0.2\ ^{+0.19}_{-0.17} \times 10^{22}$ cm^{-2}, for $\mathrm{AGN}_{1\ \mathrm{OBS}}$ and $\mathrm{AGN}_{4\ \mathrm{OBS}}$, respectively. The N_{H} values measured indicate poor obscuration towards the AGN. The detection of an emission line at $E_{\mathrm{line}} = 7.26^{+3.63}_{-1.33}$ keV however, is consistent with an iron Kα emission line, indicating higher absorption than what we measured. Annuar et al. (2020) also detected the same emission line, and found that the AGN in NGC 660 is indeed heavily obscured (potentially Compton-thick), with $\log N_{\mathrm{H}} \gtrsim 23.78\,\mathrm{cm}^{-2}$. The lower N_{H} values measured in this work are highly likely to be attributed to the usage of limited and low energy X-ray data in our analysis, in contrast with more reliable broadband X-ray spectral fittings (0.5–30 keV) performed by Annuar et al. (2020) utilizing data from both *Chandra* and *NuSTAR* observations.

Although we obtained significantly lower count rate and luminosity in the 2003 observation as compared to the other four observations in our previous analysis, the luminosities obtained from our spectroscopic analysis using the combined data indicated consistent values between $\mathrm{AGN}_{1\ \mathrm{OBS}}$ and $\mathrm{AGN}_{4\ \mathrm{OBS}}$ within the statistical uncertainties, i.e., $\log 39.03^{+0.13}_{-0.40}$ erg s^{-1} and $\log 39.34^{+0.06}_{-0.79}$ erg s^{-1}, respectively.

7 DISCUSSION

In this work, we have presented the *Chandra* observations of the PGR galaxy, NGC 660, in order to study the X-ray source population in the galaxy. Overall, we detected 22 XRB candidates and one AGN, with ∼ four sources likely to be background objects.

Galaxy properties such as SFR and stellar mass (SM) have been demonstrated to correlate with the number of X-ray sources residing in a galaxy (e.g., Fabbiano 2019). Therefore, we calculated the SFR and SM values for NGC 660 to investigate the relationship between the X-ray source population determined and the galaxy's properties. We calculated the SM by using the galaxy's B and V color band from SIMBAD[2] and utilizing the relationship derived by Bell et al. (2003). Based on this, we obtained an SM value of $0.45 \times 10^{10}\ M_{\odot}$. As for the SFR, we used Band 3 WISE color, $W_3 = 6.223$ mag and relationship derived by Lee et al. (2013), in which we calculated an SFR of 14.43 $\pm 0.19\ M_{\odot}\ \mathrm{yr}^{-1}$ for the galaxy.

We then compared the SFR and SM values determined with other galaxies, i.e., from the Mineo et al. (2012) study of X-ray emission from star forming galaxies. The paper presented SFR (calculated using IR and UV emission from Spitzer and GALEX data, respectively) and SM

[2] http://simbad.u-strasbg.fr/simbad/

Table 6 X-ray Spectral Fitting Results for the AGN (Source 21)

Model		PHABS*ZWABS* ZPOWERLW	PHABS*ZWABS*(ZPOWERLW+ZGAUSSIAN)
Parameter	Unit	$AGN_{1\ OBS}$	$AGN_{4\ OBS}$
$N_{\rm H}$	$\times 10^{22}$ cm^{-2}	$0.42^{+0.40}_{-0.33}$	$0.22^{+0.19}_{-0.17}$
Γ	...	$2.50^{+1.14}_{-1.00}$	$1.71^{+0.32}_{-0.30}$
$E_{\rm line}$	keV	...	$7.26^{+3.63}_{-1.33}$
log $L_{0.5-8{\rm keV}}$	erg s^{-1}	$39.03^{+0.13}_{-0.40}$	$39.34^{+0.06}_{-0.79}$
C-stat or χ^2 / d.o.f	...	39.64 / 37 (C-stat)	30.06 / 20 (χ^2)

(using near-IR from 2MASS data) for 29 star-forming galaxies (refer to table 1 in Mineo et al. 2012). The average SFR (<SFR>) and SM (<SM>) calculated based on their data are 4.76 $M_\odot$ yr^{-1} and 1.70 $\times$ 10^{10} $M_\odot$, respectively. In addition, the <SFR> calculated from the Wolter et al. (2018) study of ULXs collisional ring galaxies is 6.36 $M_\odot$ yr^{-1}. Comparing these values with ours, we can see that the SFR for PRG NGC 660 is much higher than the <SFR> for star forming galaxies and collisional ring galaxies studied by Mineo et al. (2012) and Wolter et al. (2018), respectively. The SM however is smaller than the <SM> calculated for the star forming galaxies.

In Figure 5, we compare the cumulative X-ray luminosity distributions for NGC 660 with the X-ray luminosity function found by Mineo et al. (2012) and Wolter et al. (2018), normalized to the SFR of our Galaxy. In general, the luminosity distribution of NGC 660 is relatively lower than that expected from the two studies, suggesting a deficit in X-ray sources detected. A relatively flatter slope can be seen at the lowest luminosity values for NGC 660, which is likely due to sensitivity effects.

In addition, a recent study by Kovlakas et al. (2020) determined that for an Sa-type galaxy, the number of ULXs per SFR is 0.16 $\pm$ 0.08. This should correspond to approximately two ULXs for NGC 660. On the other hand, Wolter et al. (2018) found a total of 50 ULXs in seven collisional ring galaxies. Based on this study, we should expect to find one ULX per unit SFR. This corresponds to about 14 ULXs for NGC 660. However, we did not identify any ULX candidate among the 23 X-ray sources detected in the galaxy.

Apart from SFR, metallicity (Z) has also been demonstrated to have a strong correlation with ULX population in galaxies. In general, frequency of ULX detection increases with decreasing metallicity. However, galaxies with metallicity of > 0.7 $Z_\odot$ were found to have a deficiency in the number of ULXs detected (Kovlakas et al. 2020)), i.e., half of that expected. We determined the value of metallicity for NGC 660 relying on oxygen abundances 12 + log (O/H) = 8.36 $\pm$ 0.08 from Egorov & Moiseev (2019) and solar oxygen abundances 12 + log (O/H) = 8.91 from Kunth & Östlin (2000). We obtained a metallicity of Z = 0.94 $\pm$ 0.01 $Z_\odot$. Based on this and the number of ULXs expected from its SFR, we should still be able to observe between about 1-7 ULX(s) in the galaxy. The fact that we detected no ULX suggests a significant deficiency in the source.

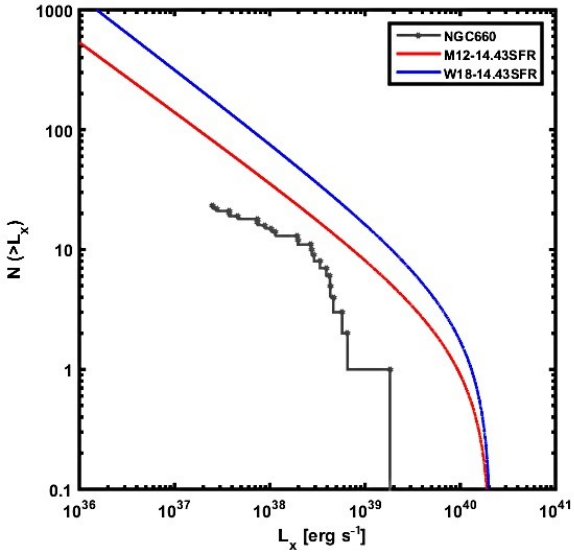

Fig. 5 Cumulative X-ray luminosity distribution for NGC 660 shown in grey. The distribution includes potential background sources ($\sim$ 4 sources) and are not corrected for incompleteness. The latter explains the relatively flatter curve observed at the lowest luminosity values. XLF obtained by Mineo et al. (2012) and Wolter et al. (2018), normalized to the SFR of NGC 660, are shown in red and blue lines, respectively.

Many studies have suggested that the deficit in the number of X-ray sources detected can be due to the presence of a compact disk and high column of gas and dust in the galaxies. This can cause significant obscuration towards X-ray sources residing in the galaxies (e.g., Smith et al. 2012 and Luangtip et al. 2015). Therefore, there is a high probability that other X-ray sources, including ULXs, exist in NGC 660, but are heavily obscured and therefore undetected. This is supported by the HR distribution of the detected sources which showed that the fainter sources have harder spectra.

8 CONCLUSION

In this paper, we analyzed *Chandra* observations of the nearby PRG NGC 660 in order to study the X-ray source population in the galaxy. Overall, we detected a total of 23 X-ray sources in the $0.5-8$ keV band. Twenty-two of these sources are located off-nuclear and have luminosities below $L_{0.5-8\ \mathrm{keV}} = 10^{39}$ erg s^{-1}, suggesting that they are likely to be XRB candidates. The remaining one source is located at the center of the galaxy, suggesting an AGN. However, we estimated that four of the detected sources could be associated with background objects. On the basis of the source count rates in each observation, we found evidence for variability for nine of the sources, including the AGN. However, further analysis using spectral modeling suggested no significant differences in the AGN luminosities between the observations. The X-ray luminosity distribution of the galaxy was found to be relatively lower than that expected from past studies on star forming and collisional ring galaxies. No ULX was also detected in the galaxy, in contrast with what is expected from the galaxy's SFR and metallicity. These results suggest a lack of X-ray sources detected in the galaxy. However, the HR distribution of the detected objects indicated that the fainter sources have harder spectra. This suggests that there could be more X-ray sources that were not detected in the galaxy due to obscuration.

Acknowledgements We would like to thank the Ministry of Higher Education Malaysia for funding this research under the Fundamental Research Grant Scheme code FRGS/1/2019/STG02/UKM/02/7. The scientific results reported in this article are based on observations made by the *Chandra* X-ray Observatory and data obtained from the *Chandra* Data Archive. This research has made use of software provided by the *Chandra* X-ray Center (CXC) in the application packages CIAO. This research made use of the data obtained through the High Energy Astrophysics Science Archive Research Center (HEASARC) Online Service, provided by the NASA/Goddard Space Flight Center, and the NASA/IPAC Extragalactic Database (NED) operated by JPL, Caltech under contract with NASA.

References

Annuar, A., Alexander, D. M., Gandhi, P., et al. 2020, MNRAS, 497, 229
Argo, M. K., van Bemmel, I. M., Connolly, S. D., & Beswick, R. J. 2015, MNRAS, 452, 1081
Baillard, A., Bertin, E., de Lapparent, V., et al. 2011, A&A, 532, A74
Bell, E. F., McIntosh, D. H., Katz, N., & Weinberg, M. D. 2003, ApJS, 149, 289
Bozzo, E., Pavan, L., Ferrigno, C., et al. 2012, A&A, 544, A118
Ducci, L., Sasaki, M., Haberl, F., & Pietsch, W. 2013, A&A, 553, A7
Egorov, O. V., & Moiseev, A. V. 2019, MNRAS, 486, 4186
Fabbiano, G. 2019, X-Rays from Galaxies, eds. B. Wilkes & W. Tucker, The Chandra X-ray Observatory (UK: IOP Publishing), 7
Goulding, A. D., & Alexander, D. M. 2009, MNRAS, 398, 1165
Jarrett, T. H., Chester, T., Cutri, R., et al. 2003, AJ, 125, 525
Kalberla, P. M. W., Burton, W. B., Hartmann, D., et al. 2005, A&A, 440, 775
Kovlakas, K., Zezas, A., Andrews, J. J., et al. 2020, MNRAS, 498, 4790
Kunth, D., & Östlin, G. 2000, A&A Rev., 10, 1
Lee, J. C., Hwang, H. S., & Ko, J. 2013, ApJ, 774, 62
Liu, Z., O'Brien, P. T., Osborne, J. P., et al. 2019, MNRAS, 486, 5709
Lu, N. Y., Hoffman, G. L., Groff, T., et al. 1993, ApJS, 88, 383
Luangtip, W., Roberts, T. P., Mineo, S., et al. 2015, MNRAS, 446, 470
Luo, B., Brandt, W. N., Xue, Y. Q., et al. 2017, VizieR Online Data Catalog, J/ApJS/228/2
Mineo, S., Gilfanov, M., & Sunyaev, R. 2012, MNRAS, 419, 2095
Mineo, S., Rappaport, S., Levine, A., et al. 2014, ApJ, 797, 91
Mosenkov, A. V., Baes, M., Bianchi, S., et al. 2018, VizieR Online Data Catalog, J/A+A/622/A132
Reshetnikov, V. P., Faúndez-Abans, M., & de Oliveira-Abans, M. 2011, Astronomy Letters, 37, 171
Reshetnikov, V. P., & Mosenkov, A. V. 2019, MNRAS, 483, 1470
Ricci, C., Trakhtenbrot, B., Koss, M. J., et al. 2017, ApJS, 233, 17
Roberts, T. P., Warwick, R. S., Ward, M. J., & Murray, S. S. 2002, MNRAS, 337, 677
Sanchez, M., & Rangelov, B. 2019, in American Astronomical Society Meeting Abstracts, 233, 464.05
Sharma, P., Sharma, R., Jain, C., & Dutta, A. 2020, MNRAS, 496, 197
Smirnova, K. I., Wiebe, D. S., & Moiseev, A. V. 2017, Open Astronomy, 26, 88
Smith, B. J., Swartz, D. A., Miller, O., et al. 2012, AJ, 143, 144
van Driel, W., Combes, F., Casoli, F., et al. 1995, AJ, 109, 942
Vulic, N., Hornschemeier, A., Yukita, M., et al. 2020, in American Astronomical Society Meeting Abstracts, 235, 430.09
Whitmore, B. C., Lucas, R. A., McElroy, D. B., et al. 1990, AJ, 100, 1489
Wolter, A., Fruscione, A., & Mapelli, M. 2018, ApJ, 863, 43
Zadorozhna L. V., Tugay A. V., & Shevchenko S. Yu. 2020, Astronomical School's Report, 16, 1